





Unveiling the mechanism of spin to charge conversion in the ferroelectric topological crystalline insulator SnTe

E. C. Souza ^{1,*}, J. E. Abrão ¹, M. A. Correa,² F. Bohn ², M. Gamino ² and S. M. Rezende¹

¹*Departamento de Física, Universidade Federal de Pernambuco, 50670–901, Recife, Pernambuco, Brazil*

²*Departamento de Física, Universidade Federal do Rio Grande do Norte, 59078–900, Natal, RN, Brazil*



(Received 25 January 2024; revised 30 June 2024; accepted 2 July 2024; published 31 July 2024)

The ferroelectric topological crystalline insulator SnTe is a promising material for ferronics and spintronics studies and applications because of the strong spin-orbit coupling and surface states protected by the mirror symmetry of the crystal. In this paper, we report ferromagnetic resonance-driven spin-pumping experiments in several bilayers and trilayers having one layer of SnTe with thickness varying in the range 3–30 nm and different ferromagnetic layers used to inject the spin-pumped spin current. In all samples x-ray-diffraction spectra strongly indicate that the SnTe films grown are topological crystalline insulators and consequently have preserved topological surface states. The spin-pumping studies reveal that the dominant spin to charge conversion mechanism in SnTe is the inverse Rashba-Edelstein effect (IREE), evidencing that the topological surface states are preserved. From the data in all samples, we obtain for the IREE parameter values in the range 1.1–2.8 pm, which are comparable to the ones measured in graphene, Bi₂Se₃, and others topological insulators.

DOI: [10.1103/PhysRevB.110.014444](https://doi.org/10.1103/PhysRevB.110.014444)

I. INTRODUCTION

Magnetic materials are at the root of the field of spintronics that has been one of the most active areas of research in magnetism in the last two decades [1–13]. In many areas of this field the elementary excitations of the spins, called spin waves or magnons, play an essential role in the mechanism of intricate phenomena, such as the spin Seebeck effect [14–24]. The fact that magnetism and ferroelectricity break, respectively, time-reversal and space-inversion symmetry [25,26], has stimulated proposals of analogies of phenomena in the two areas. While in magnets the magnetic dipoles order below some critical temperature, in ferroelectrics, the ordering occurs with the electric dipoles, also below some critical temperature. Recently it has been proposed that the elementary excitations of the electric polarization in ferroelectric materials, which have been called ferrons, might play a role similar to magnons in some phenomena in nanostructures [27–32].

One class of ferroelectrics that has been attracting attention falls in the category of topological insulators (TIs), which are characterized by the emergence of surface metallic states. These are called topological surface states, which exhibit peculiar properties such as massless fermions on the Dirac-shape band dispersion, and spin-momentum locking [33–39]. One important material of this class is SnTe, which is semiconducting at room temperature [40–45]. Furthermore, its designation as a topological crystalline insulator is highlighted by the manifestation of crystal symmetry-protected topological surface states [45–47]. These surface states exhibit metallic characteristics, featuring an intriguing arrangement of an even number of Dirac cones on high-symmetry

crystal surfaces such as {001}, {110}, and {111} [33,36]. This distinctive electronic configuration imparts SnTe with remarkable properties, making it a subject of intense studies and explorations. Moreover, SnTe distinguishes itself as a novel multifunctional material, referred to as ferroelectric Rashba semiconductor [48]. The moniker stems from the material's unique combination of ferroelectric and Rashba spin-splitting properties. These properties grant SnTe the ability to have a controllable and switchable spin texture via an electric field [49]. This groundbreaking characteristic opens up avenues for applications in ferronics and spintronics indicating potential links between topology and Rashba physics within the same category of materials [49]. A few years ago, this material was used in epitaxial Fe/SnTe multilayer structures to study spin to charge current conversion in spin-pumping experiments driven by ferromagnetic resonance [43]. By examining the dependence of the measured voltage on the microwave power, magnetic-field angle, and temperature, the authors concluded that the conversion mechanism takes place in bulk SnTe by means of the inverse spin Hall effect (ISHE) [50–54].

In this paper we report an investigation of the spin to charge current conversion in SnTe by means of the microwave spin-pumping technique [54–59]. We have used four different heterostructures, a simple bilayer of YIG/SnTe (YIG-Y₃Fe₅O₁₂, yttrium iron garnet), a reference sample of YIG/Pt/Py (Py-permalloy-Ni₈₁Fe₁₉), a trilayer of YIG/SnTe/Py, and a trilayer of Co/SnTe/Py. The magnetization precession produced by microwave-driven ferromagnetic resonance (FMR) in the ferromagnetic (FM) layer creates a pure spin current that flows across the interface with SnTe and it is converted into a transversal charge current that is detected as a dc voltage between two edge contacts. Our results show that by changing the direction of the pumped spin current, we

*Contact author: edycleyson.souza@ufpe.br

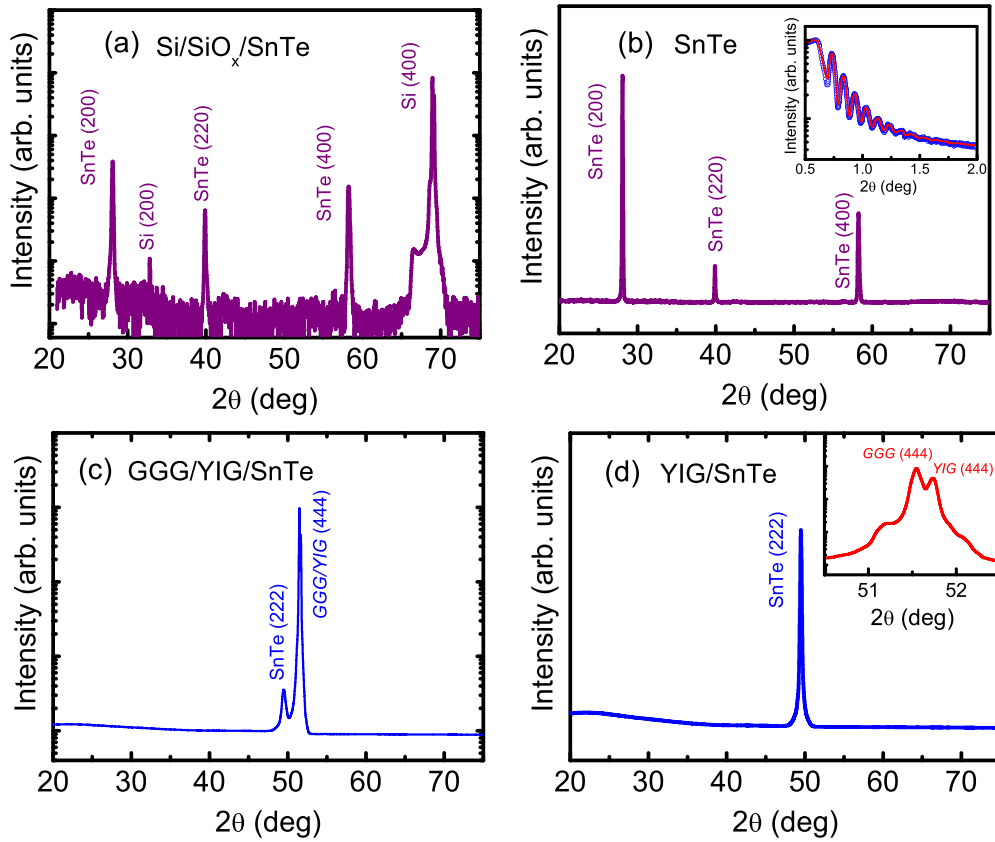


FIG. 1. (a) Out-of-plane XRD patterns (θ - 2θ scans) of SnTe (30 nm) film grown on a Si (100) substrate. (b) GIXRD pattern of the Si/SnTe (30-nm) sample. The inset of (b) shows the XRR for a 30-nm-thick SnTe. The red solid line across the XRR data is the best fitting for the calibration thickness and surface roughness. (c) XRD patterns (θ - 2θ scans) of SnTe (30 nm) film grown on a GGG/YIG (111) sample. (d) GIXRD pattern of the YIG/SnTe (30 nm) sample. The inset of (d) shows Bragg diffraction of the GGG substrate and the epitaxial YIG in the (444) planes.

ascertain that the dominant spin charge conversion mechanism in SnTe thin films is not ISHE, but rather the IREE [60–85].

II. SAMPLE PREPARATION AND CHARACTERIZATION

The YIG ($\text{Y}_3\text{Fe}_5\text{O}_{12}$) films were grown onto GGG (111) ($\text{Ga}_3\text{Gd}_5\text{O}_{12}$) substrate via liquid-phase epitaxy. High-purity oxides of Fe_2O_3 , Y_2O_3 , PbO , and B_2O_3 , were mixed into a Pt crucible at a temperature of 1000°C , and the mixing process was done until reaching a homogeneous melt. The melt was then cooled down to the temperature of 935°C at which the films were grown. The thickness of the YIG films grown onto GGG substrate was 100 nm. Once the YIG films was grown, the film was cut into $3.0 \times 2.0\text{-mm}^2$ samples; following, the samples were cleaned in an ultrasonic bath with acetone. The Pt and SnTe layers were deposited at room temperature by dc magnetron sputtering. The deposition process was carried out with base pressure of 2.0×10^{-7} Torr, deposition pressure of 3.0 mTorr with a 99.99% pure Ar at 32-sccm constant flow and setting 60 W in the power source. Moreover, the Permalloy and cobalt layers were prepared by dc magnetron sputtering in a similar way.

The structural properties were measured through x-ray diffraction (XRD) using a Rigaku x-ray diffractometer, model Smartlab, with the CuK_α radiation ($\lambda = 1.5418 \text{ \AA}$) in a θ - 2θ Bragg-Brentano geometry. Figure 1(a) shows the out-of-plane

XRD θ - 2θ scan pattern of the Si/SiO_x/SnTe (30-nm) sample. The SnTe spectra become more evident when the substrate contribution is subtracted out using the grazing incidence x-ray-diffraction (GIXRD) technique, as shown in Fig. 1(b). This technique is used to minimize the diffraction intensity that comes from the Si substrate, thus emphasizing the characteristic peaks of SnTe films. Clearly, the diffraction peaks of the SnTe layers are preferentially oriented along the (100) and (110) planes, exhibiting reflections associated with the (200) and (220) crystalline planes at $2\theta = 28.14^\circ$ and $2\theta = 58.32^\circ$, respectively.

The thickness calibration as well as the surface roughness of the SnTe films were estimated using x-ray reflectivity (XRR). The well-defined Kiessig fringes for a 30-nm-thick SnTe are shown in the inset of Fig. 1(b). Figure 1(c) shows the XRD pattern for the GGG/YIG (100-nm)/SnTe (30-nm) sample with a diffraction peak associated with the (444) crystal plane of YIG and SnTe (222). The GIXRD data in Fig. 1(d) show a narrow diffraction peak characteristic of the SnTe film, at $2\theta \approx 49^\circ$. This feature observed for the YIG/SnTe sample indicates that the SnTe layers grown onto GGG/YIG (111) provide well-textured behavior along {111} directions. From high-resolution XRD measurements shown in the inset of Fig. 1(d), we can observe the two peaks at $2\theta \approx 51.10^\circ$ and $2\theta \approx 51.23^\circ$, corresponding to the (444) Bragg diffractions of the GGG substrate and the epitaxial YIG in the (444) plane,

respectively. With regards to the XRD results, is important to note that the topological nature of electronic structures of the SnTe arises from crystalline symmetry. Unlike conventional topological insulators, in which the surface topology is easily broken due to magnetic perturbation when a ferromagnetic material is grown onto topological insulators, the SnTe surface topology is protected due to the high crystalline symmetry that is associated with the $\{001\}$, $\{110\}$, and $\{111\}$ directions. Thus, the x-ray results strongly indicate that the SnTe films are topological crystalline insulators and consequently have preserved topological surface states.

III. SPIN-PUMPING EXPERIMENTS IN BILAYERS WITH SnTe

Ferromagnetic resonance measurements were carried out in a homemade X-band microwave spectrometer. The sample was mounted on the tip of a polyvinyl chloride (PVC) rod and inserted into a rectangular microwave cavity operating in the TE_{102} mode, with resonance frequency of 9.417 GHz, quality factor (Q_L) of 2000. In order to avoid rf electric effects, the samples were placed close to the end wall of the cavity, in a nodal position of minimum rf electric field and maximum rf magnetic field perpendicular to the static field, such that the rf magnetic field drove the magnetization precession. This precaution avoided the generation of galvanic effects caused by the rf electric field. The static magnetic field produced by the poles of an electromagnet were modulated at 1.2 kHz with a pair of Helmholtz coils that allowed lock-in detection of the absorption derivative.

The spin-pumping experiments were carried out using samples made of one film of SnTe with varying thickness (t) in contact with three different magnetic films, ferrimagnetic YIG and ferromagnetic Co and Py. The YIG/SnTe (t) bilayers were used to quantify the spin to charge conversion efficiency. In order to investigate the behavior of the voltage polarities with inversion of the spin current direction to show that the mechanism of the spin-to-charge conversion in SnTe was IREE, we used trilayer samples of YIG/SnTe/Py and Co/SnTe/Py. In the spin-pumping experiment, the FM film in the multilayer sample was subjected to a rf magnetic field with frequency in the microwave range applied perpendicularly to a static field so as to drive the magnetization precession about the field. At the interface with a conducting layer, the precessing spins in the FM film generated a spin current that flowed into the adjacent layer and produced two effects: (i) Increased damping of the magnetic excitation due to the flow of spin angular momentum out of the FM film [56,78]; and (ii) Generation of a charge current by means of a spin to charge conversion mechanism that produced a voltage at the ends of the layer, as sketched in Fig. 2(a). These two independent phenomena made possible the extraction of material parameters from the measurements of the FMR absorption and the spin-pumping voltage.

Figure 3(a) shows the FMR spectrum of a bare 100-nm-thick YIG film, obtained with H in plane and normal to the long strip dimension, with microwave frequency $f = 9.417$ GHz and input power $P = 20$ mW. The absorption line corresponds to the uniform (FMR) mode that has frequency close to the spin-wave mode with $k = 0$, given by the Kittel equation $\omega_0 \approx \gamma H^{1/2}(H + 4\pi M_{\text{eff}})^{1/2}$, where

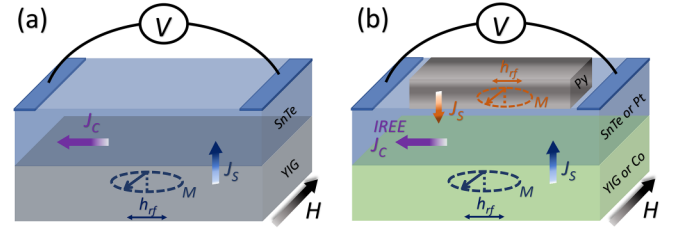


FIG. 2. (a) Sketch of the YIG/SnTe and (b) YIG (or Co)/SnTe/Py samples used in the FMR-driven spin-pumping experiments. The lateral dimensions are 3.0×2.0 mm².

$\gamma = 2\pi \times 2.8$ GHz/kOe is the gyromagnetic ratio for YIG, and $4\pi M_{\text{eff}}$ is the effective magnetization. The fit of the line with a Lorentzian derivative function, shown in Fig. 3(a), provides the half width at half maximum, or simply linewidth, of $\Delta H = 5.1$ Oe.

Figures 3(b)–3(d) show the FMR absorption derivative spectra of three of the four YIG/SnTe (t) bilayers studied here, with the SnTe layer thickness t indicated. Clearly, in all samples the FMR linewidth was larger than the one of the bare YIG film. This was attributed to the spin-pumping damping, resulting from the precession of the magnetization \vec{M} in the YIG film, which generated a spin current at the YIG/SnTe interface with density

$$\vec{J}_S = \frac{\hbar g_{\text{eff}}^{\uparrow\downarrow}}{4\pi M^2} \left(\vec{M} \times \frac{\partial \vec{M}}{\partial t} \right), \quad (1)$$

where $g_{\text{eff}}^{\uparrow\downarrow}$ is the real part of the interface spin-mixing conductance, which takes into account the spin-pumped and backflow spin currents [57,78,79]. The spin current that flows into the adjacent conducting layer produces increased damping of the magnetic excitation due to the flow of spin angular momentum out of the FM film. The additional linewidth due to the spin-pumping mechanism is given by [78]

$$\Delta H_{\text{SP}} = \frac{\hbar \omega g_{\text{eff}}^{\uparrow\downarrow}}{4\pi M t_{\text{FM}}}, \quad (2)$$

where ω is the driving frequency, t_{FM} is the thickness of the FM layer, and SP is spin pumping. Actually, this expression is valid for relatively thin FM films, with thickness smaller than a coherence length. For thicker films it has been shown that the thickness in Eq. (2) has to be replaced by a coherence length that for YIG is on the order of 300 nm [79]. By measuring the linewidths before and after the deposition of the SnTe layer on the same sample as in Refs. [59,65,72], one can extract a reliable value for the spin-mixing conductance with a simple relation obtained from Eq. (2) [78,79],

$$g_{\text{eff}}^{\uparrow\downarrow} = \frac{4\pi M t_{\text{FM}}}{\hbar \omega} (\Delta H_{\text{FM/ML}} - \Delta H_{\text{FM}}). \quad (3)$$

Using this relation and the measured linewidths shown in Fig. 3, we obtained for the four YIG/SnTe bilayers similar values for the spin-mixing conductance. The average value was $g_{\text{eff}}^{\uparrow\downarrow} \approx 3 \times 10^{17}$ m⁻², which was somewhat smaller than the values measured in YIG/Pt interfaces [55–59].

For the investigation of the spin-pumping voltage V_{SP} , two Cu electrodes were attached with silver paint to the edges of the SnTe layer, as depicted in Fig. 2(a), and con-

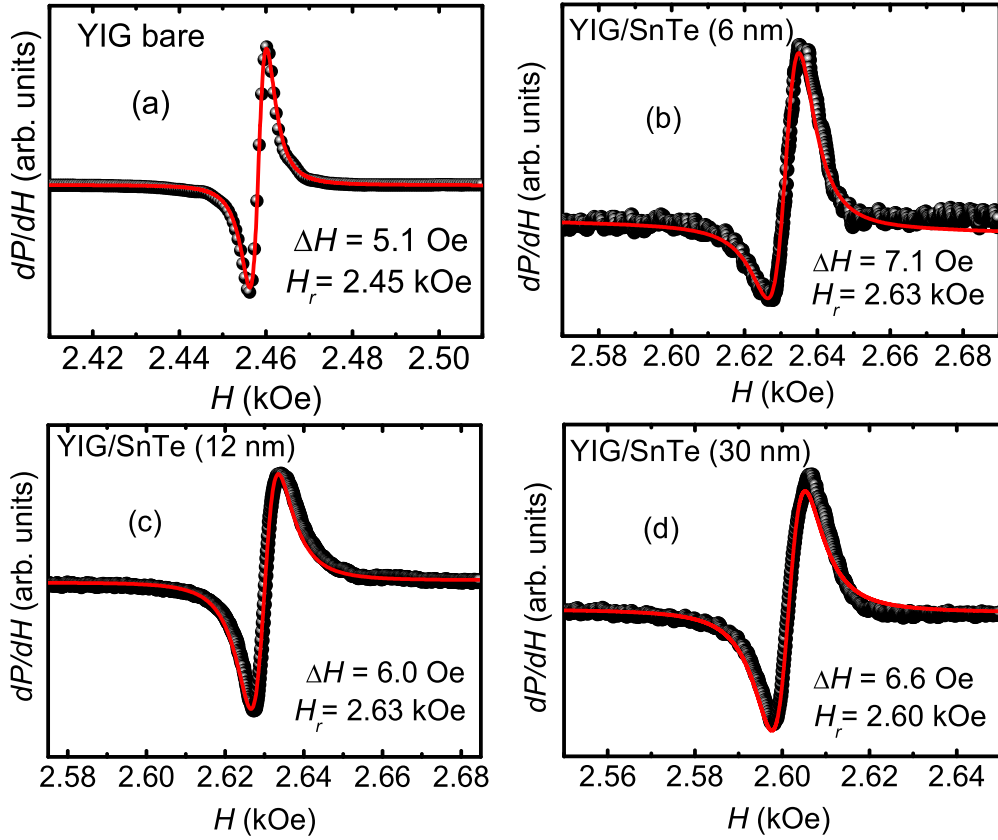


FIG. 3. Field-scan FMR microwave absorption derivative spectra measured at a frequency of 9.417 GHz with the magnetic field applied in the film plane, normal to the long dimension: (a) Bare YIG (100 nm) film; (b)–(d) YIG/SnTe bilayers for several SnTe layer thickness. The (red) solid lines across the FMR data for all samples are the best fittings using a Lorentzian derivative function.

nected directly to a nanovoltmeter. As mentioned earlier, the sample was mounted on the top of a polyvinyl chloride (PVC) rod and inserted in a hole at the end wall of the microwave cavity so that it could be rotated while maintaining the static and rf fields in the sample plane and perpendicular to each other. The measurements were made at an in-plane fixed angle ϕ of the field relative to the axis perpendicular to the electrodes along the sample, without the ac field modulation, sweeping the field to obtain a spectrum of $V_{SP}(H)$. Figure 4 shows the spectra of the spin-pumping voltage V_{SP} measured in the four YIG/SnTe samples, with a microwave frequency of 9.417 GHz and power of 110 mW, for three directions of the field, $\phi = 0^\circ$, 90° , and 180° . As expected, at $\phi = 0^\circ$ all samples exhibited a peak in the spin-pumping voltage at the field of resonance, as in Fig. 3. The peak reversed polarity if the sample was rotated to $\phi = 180^\circ$, and the signal vanished for $\phi = 90^\circ$. This behavior was common to the two known mechanisms for spin to charge conversion, ISHE and IREE. However, one notable feature of the data in Fig. 4 is that while the spin-pumping voltage was negative for $\phi = 0^\circ$, in the well-studied YIG/Pt bilayer, at $\phi = 0^\circ$ it was positive [21,80].

Figure 5 shows another important feature of both conversion mechanisms, a linear variation of the spin-pumping current peak, $I_{SP} = V_{SP}/R$ (R is resistance measured between the two contacts) with the microwave power, measured in all four YIG/SnTe samples.

IV. SPIN PUMPING IN TRILAYERS AND INTERPRETATION OF THE DATA

In order to investigate the mechanism of spin to charge conversion in SnTe, we have carried out spin-pumping experiments with trilayers, in which a nonmagnetic conducting layer was sandwiched between two different FM films, as depicted in Fig. 2(b). This arrangement made possible to inject a spin-pumped spin current from either side of the conducting layer in order to verify the behavior of the spin-pumping voltage polarity with the inversion of the spin current direction. In case the spin to charge conversion is the inverse spin Hall effect (ISHE), a spin current with density \vec{J}_S pumped by a FM film into the conducting layer, the charge current density generated in the conversion process is [53–56]

$$\vec{J}_C = \theta_{SH}(2e/\hbar)(\vec{J}_S \times \hat{\sigma}), \quad (4)$$

where $\hat{\sigma}$ is the spin polarity of the spin current and θ_{SH} is the spin Hall angle. Equation (4) shows an important feature of the ISHE mechanism: the direction of the charge current, and thus the sign of the spin-pumping voltage, reverses either with the reversal in the direction of the spin current, or the direction of the spin polarity. This is the case for a conducting layer made of platinum, which is a well-known material in which the spin to charge conversion mechanism is the ISHE [21,80,81]. Figure 6(a) shows that in the YIG/Pt (6-nm)/Py (30-nm) trilayer, the peak of V_{SP} corresponding to the FMR in

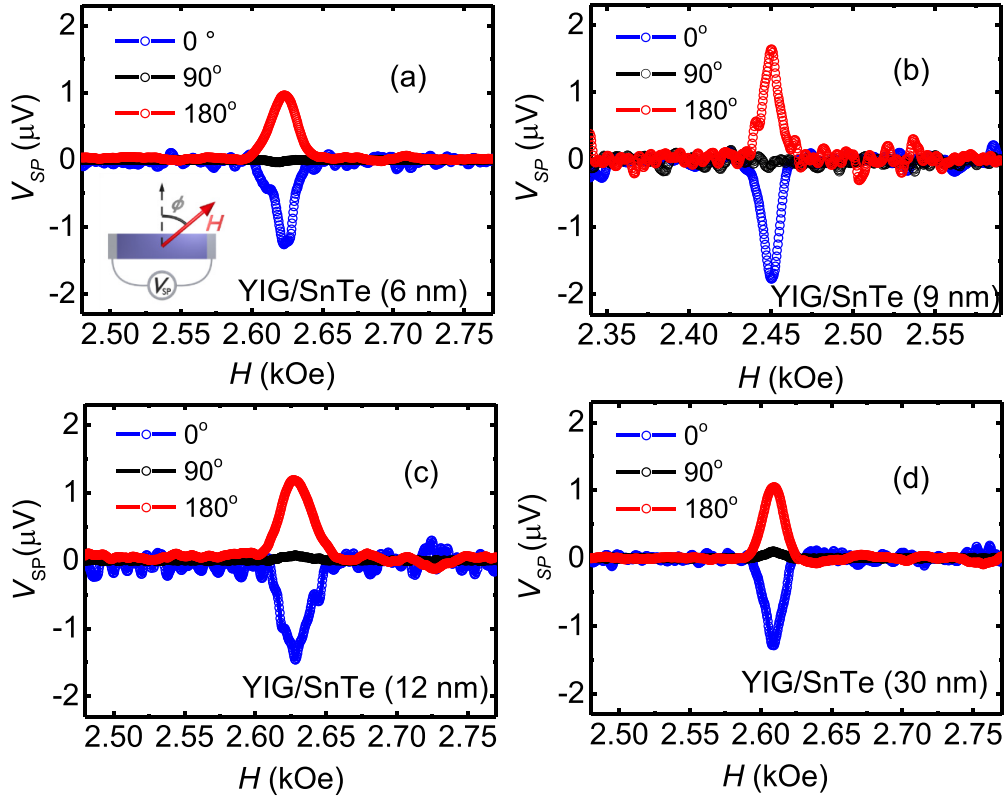


FIG. 4. Field scan spin pumping DC voltage measured with microwave driving with frequency 9.417 GHz and power 110 mW for (a) YIG/SnTe (6 nm), (b) YIG/SnTe (9 nm), (c) YIG/SnTe (12 nm), and (d) YIG/SnTe (30 nm) bilayers, with the magnetic field applied in the film plane at the angles ϕ indicated. The inset in (a) shows the definition of the angle ϕ between the field and the axis normal to the long sample dimension.

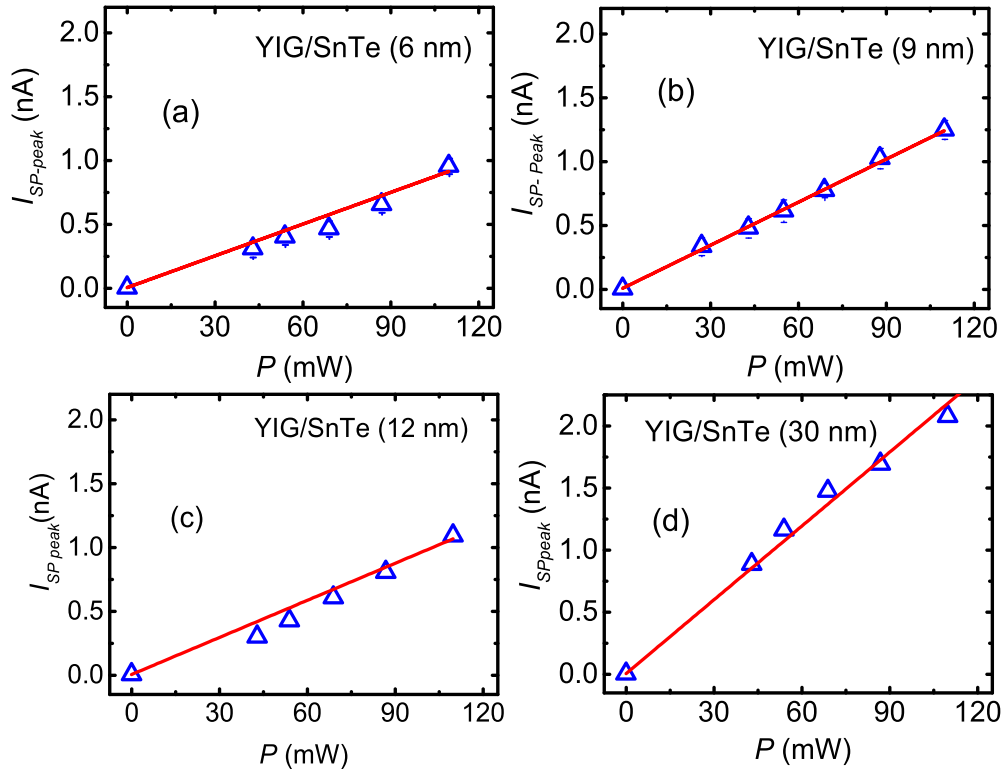


FIG. 5. Variation of the spin-pumping current peak with the FMR microwave driving power measured with frequency 9.417 GHz for (a) YIG/SnTe (6 nm), (b) YIG/SnTe (9 nm), (c) YIG/SnTe (12 nm), and (d) YIG/SnTe (30 nm).

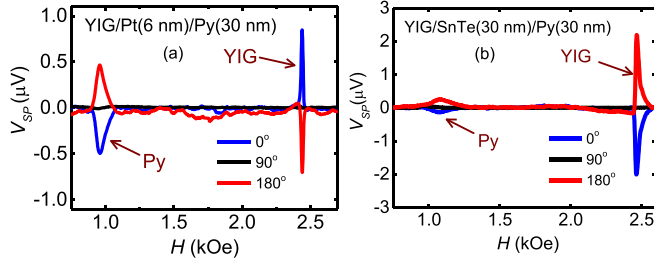


FIG. 6. Field-scan spin-pumping voltages in the SnTe conducting layer sandwiched between two FM films produced by FMR at 9.417 GHz. (a) YIG/Pt (6 nm)/Py (30 nm). (b) YIG/SnTe (30 nm)/Py (30 nm).

Py, at $H_r = 0.96$ kOe, has the opposite sign as the peak due to the FMR in YIG at $H_r = 2.45$ kOe, because the spin currents injected by Py and by YIG have opposite directions. Also, both peaks change sign when the magnetic field is reversed, because this reverses the direction of the spin polarity $\vec{\sigma}$.

In case the spin to charge conversion is dominated by the inverse Rashba-Edelstein effect (IREE), a spin current with density \vec{J}_S pumped by either FM film into a 2D conducting layer, the surface charge current density generated in the conversion process can be written as [63,68,77]

$$\vec{J}_C = \alpha_R (e/\hbar) (\hat{z} \times \vec{S}), \quad (5)$$

where α_R is Rashba parameter, \vec{S} is nonequilibrium spin density due to spin injection, and \hat{z} is the unit vector normal to the interface. Equation (5) shows that in contrast to the case of ISHE, the sign of the IRRE charge current does not change with the reversal of the spin current direction. Thus, if the IRRE is the dominant mechanism for the spin-charge conversion, one expects voltage signs for the two peaks corresponding to spin pumping from the FMR films on the two sides of the conducting layer to have the same polarity [76,77]. This is just what occurs in the trilayer of YIG/SnTe

(30 nm)/Py (30 nm), that has spin-pumping voltage shown in Fig. 6(b) for three directions of the magnetic field, $\phi = 0^\circ$, 90° , and 180° . The spectra exhibit two peaks, one at $H_r = 0.95$ kOe, due to the FMR in Py, and another one at $H_r = 2.6$ kOe, corresponding to the spin current generated by the FMR in YIG. Clearly, for either $\phi = 0^\circ$ or 180° , the two peaks have the same sign, in contrast to the behavior in YIG/Pt/Py.

These results represent very strong indication that the spin-to-charge conversion mechanism in SnTe is the IREE, not ISHE as reported in Ref. [43]. In order to confirm this conclusion, we have carried out spin-pumping measurements in trilayers of Pt or SnTe sandwiched between two different metallic FM films, Co and Py. Fig. 7 shows the FMR absorption derivative spectra and the spin-pumped voltage of three samples, Co (20 nm)/Pt (4 nm)/Py (20 nm), and Co (20 nm)/SnTe (3 nm)/Py (20 nm), and Co (20 nm)/SnTe (30 nm)/Py (20 nm). The FMR lines in Figs. 7(a), 7(b), and 7(c) with resonance fields at ~ 0.6 kOe and ~ 1.0 kOe correspond, respectively, to the Co and Py films. The behavior of the spin-pumping voltage peaks in Figs. 7(d), 7(e), and 7(f) is similar to the one observed in YIG/Pt/Py and YIG/SnTe/Py. The H dependence of V_{SP} for Co/SnTe/Py layers shows a symmetric Lorentzian line shape with a minimal antisymmetric component, as shown in Refs. [55,63,83,84]. This indicates that the contributions from galvanomagnetic and spin rectification effects, produced by the metallic layers itself [59], can be neglected. While in the first sample the two peaks arising from spin currents injected from opposite directions have opposite signs, in the second and third samples they have the same sign. We have also made these measurements in other Co/SnTe (t)/Py samples with thickness $t = 6, 9$, and 12 nm, and obtained very similar results. Therefore, these results demonstrate clearly that also with spin pumping produced by FMR in metallic films, the spin to charge conversion mechanism in SnTe is the IREE, not ISHE.

Taking the previous results, let us calculate the IRRE parameter for the SnTe first using the spin-pumping data

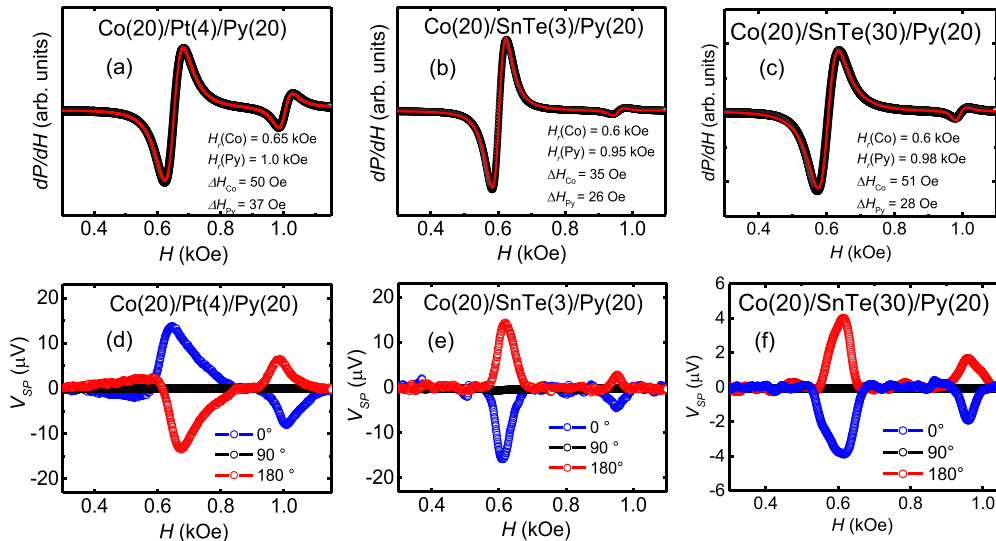


FIG. 7. Field-scan FMR absorption measured at 9.4 GHz in (a) Co (20 nm)/Pt (4 nm)/Py (20 nm), (b) Co (20 nm)/SnTe (3 nm)/Py (20 nm), and (c) Co (20 nm)/SnTe (30 nm)/Py (20 nm). (d), (e), (f) Spin-pumping voltages in the conducting layer sandwiched between the Co and Py films produced by FMR in the same samples.

obtained with the YIG/SnTe (t) because YIG is an insulator so that the measured resistances are due solely due the SnTe layer. As is well established, the spin current density at the YIG/SnTe interface generated by the magnetization precession is, in units of angular momentum–time area [21,55,56],

$$J_S = \frac{\hbar\omega p_{xy} g_{\text{eff}}^{\uparrow\downarrow}}{4\pi} \left(\frac{h_{\text{rf}}}{\Delta H} \right)^2 L(H - H_r), \quad (6)$$

where $\omega = 2\pi f$ and h_{rf} are, respectively, the frequency and amplitude of the driving microwave magnetic field, $L(H - H_r)$ denotes a Lorentzian function, H_r is the field for resonance, and p is the magnetization precession ellipticity factor given by $p_{xy} = 4(\omega/\gamma)(H_r + 4\pi M_{\text{eff}})/(2H_r + 4\pi M_{\text{eff}})^2$, where $4\pi M_{\text{eff}}$ is the effective magnetization that appears in the expression for the FMR frequency $f = \gamma [H_r(H_r + 4\pi M_{\text{eff}})]^{1/2}$. For YIG, at 9.4 GHz, the ellipticity factor is $p_{xy} = 0.31$.

The spin current in Eq. (6) is injected in the SnTe layer where it is converted into a surface charge current with density j_c given by Eq. (5). Using Eq. (5) in the form $J_c = \alpha_R(e/\hbar)\langle\delta_s\rangle$ and spin current density $J_c/e = \langle\delta_s\rangle/\tau_s$, as reported [63], where τ_s is an effective relaxation time, charge current density can be written as $j_c = (2e/\hbar)\lambda_{\text{IREE}} J_S$ in units of charge/(time \times area), where e is the electron charge and $\lambda_{\text{IREE}} = \alpha_R(\tau_s/\hbar)$ is called the IREE parameter. Using the relation in $V_{\text{IREE}} = R w j_c$, where R and w are, respectively, the resistance and lateral width of the SnTe layer, we obtain an expression for the IREE parameter in terms of the measured voltage peak value:

$$\lambda_{\text{IREE}} = \frac{4V_{\text{IREE}}^{\text{peak}}}{R w e f g_{\text{eff}}^{\uparrow\downarrow} p_{xy} (h_{\text{rf}}/\Delta H)^2}. \quad (7)$$

The driving rf magnetic field at the back wall of a rectangular waveguide cavity is calculated with an expression obtained for the electromagnetic fields in the TE₁₀₂ mode [82]:

$$h_{\text{rf}} = \left[Q_L(\varepsilon_0/\mu_0)^{1/2} \left(\frac{8}{\pi ab} \right) \left(1 - \frac{\lambda_0^2}{4a^2} \right)^{3/2} \right]^{1/2} P^{1/2}, \quad (8)$$

where P is the microwave power, λ_0 , a , and b are, respectively, the wavelength in vacuum and the two inner waveguide dimensions, ε_0 and μ_0 are the vacuum permittivity and permeability, and Q_L is the quality factor of the loaded cavity. Using the dimensions for an X-band waveguide, one can show that for $f = 9.417$ GHz and $Q_L = 2000$, the amplitude of the driving field in Oe units is given by $h_{\text{rf}} = 1.776(P)^{1/2}$, where

P is the input power in watts. For $P = 110$ mW this gives $h_{\text{rf}} = 0.56$ Oe.

Using for the four YIG/SnTe (t) bilayers with thicknesses $t = (6, 9, 12, 30)$ nm investigated here, the values of the respective spin-mixing conductance determined by Eq. (2) using the measured linewidths, $g_{\text{eff}}^{\uparrow\downarrow} = (5.1, 6.7, 2.3, 3.8) \times 10^{17} \text{ m}^{-2}$, the resistances measured between the two contacts in the SnTe layer, $R = (1.4, 1.6, 1.2, 0.66)$ k Ω , the peak values of the spin-pumping voltages $V_{\text{SP}} = (1.3, 1.6, 1.5, 1.28) \mu\text{V}$, $f = 9.417$ GHz, $p_{xy} = 0.31$, $w = 2$ mm, and $h_{\text{rf}} = 0.56$ Oe, we obtain for the values of the IREE parameter in the four SnTe (t) layers $\lambda_{\text{IREE}} = (1.12, 1.09, 2.43, 2.82) \times 10^{-3}$ nm. Thus, we can consider for SnTe the value $\lambda_{\text{IREE}} = 1.87 \pm 0.48$ pm, which is on the same order of magnitude as graphene [65,85], Bi₂Se₃ [86], as well as other topological insulators [72,87]. Similar calculations done for SnTe in the trilayers using the data shown in Figs. 6 and 7 give IREE parameters on the same order of magnitude as in YIG/SnTe.

In summary, we have conducted ferromagnetic resonance-driven spin-pumping experiments in several bilayers and trilayers having one layer of the ferroelectric topological crystalline insulator SnTe with thickness varying in the range 3–30 nm. Our study reveals unequivocally that the spin to charge conversion mechanism in the SnTe layer for all thicknesses is the inverse Rashba-Edelstein effect (IREE). This conclusion is confirmed by comparison with measurements made in trilayers containing a platinum layer instead of SnTe. While in Pt the sign of the spin-pumping voltage changes when the injected spin current changes direction, in SnTe the sign does not vary with the direction of the spin current. From the data in all samples, we obtain for the inverse Rashba-Edelstein effect parameter λ_{IREE} values in the range 1.1–2.8 pm, which are comparable to the ones measured in graphene, Bi₂Se₃, and other topological insulators.

ACKNOWLEDGMENTS

The authors are grateful to A. Moraes for technical support. This work was supported by the Brazilian agencies Conselho Nacional de Desenvolvimento Científico e Tecnológico (CNPq), Coordenação de Aperfeiçoamento de Pessoal de Nível Superior (CAPES), Financiadora de Estudos e Projetos (FINEP), Fundação de Amparo à Promoção da Ciência, Tecnologia e Inovação do Estado do Rio Grande do Norte (FAPERN) and Fundação de Amparo à Ciência e Tecnologia do Estado de Pernambuco (FACEPE). The authors acknowledge support of the INCT of Spintronics and Advanced Magnetic Nanostructures (INCT-SpinNanoMag), CNPq Grant No. 406836/2022-1.

[1] I. Žutić, J. Fabian, and S. Das Sarma, Spintronics: Fundamentals and applications, *Rev. Mod. Phys.* **76**, 323 (2004).
 [2] G. E. W. Bauer, E. Saitoh, and B. J. van Wees, Spin caloritronics, *Nat. Mater.* **11**, 391 (2012).
 [3] D. Pesin and A. H. MacDonald, Spintronics and pseudospintronics in graphene and topological insulators, *Nat. Mater.* **11**, 409 (2012).

[4] *Recent Advances in Magnetic Insulators—From Spintronics to Microwave Applications*, edited by M. Wu and A. Hoffmann (Academic Press-Elsevier, San Diego, 2013).
 [5] T. Jungwirth, J. Wunderlich, V. Novák, K. Olejník, B. L. Gallagher, R. P. Campion, K. W. Edmonds, A. W. Rushforth, A. J. Ferguson, and P. Němec, Spin-dependent phenomena and

- device concepts explored in (Ga,Mn)As, *Rev. Mod. Phys.* **86**, 855 (2014).
- [6] A. Hoffmann and S. D. Bader, Opportunities at the frontiers of spintronics, *Phys. Rev. Appl.* **4**, 047001 (2015).
- [7] S. Bandyopadhyay and M. Cahay, *Introduction to Spintronics*, 2nd ed. (CRC Press, Boca Raton, 2015).
- [8] E. E. Fullerton and J. R. Childress, Spintronics, magnetoresistive heads, and the emergence of the digital world, *Proc. IEEE* **104**, 1787 (2016).
- [9] S. Datta, *Lessons from Nanoelectronics: A New Perspective on Transport- Basic Concepts*, 2nd ed. (World Scientific Publishing, Singapore, 2017).
- [10] S. Manipatruni, D. E. Nikonov, and I. A. Young, Beyond CMOS computing with spin and polarization, *Nat. Phys.* **14**, 338 (2018).
- [11] P. Kumar, R. Kumar, S. Kumar, M. K. Khanna, R. Kumar, V. Kumar, and A. Gupta, Interacting with futuristic topological quantum materials: A potential candidate for spintronics devices, *Magnetochemistry* **9**, 73 (2023).
- [12] Y. Zhang *et al.*, Ferrimagnets for spintronic devices: From materials to applications, *Appl. Phys. Rev.* **10**, 011301 (2023).
- [13] A. Hirohata, K. Yamada, Y. Nakatani, I.-L. Prejbeanu, B. Dieny, P. Pirro, B. Hillebrands, Review on spintronics: Principles and device applications, *J. Mag. Mag. Mat.* **509**, 166711 (2020).
- [14] K. Uchida, S. Takahashi, K. Harii, J. Ieda, W. Koshibae, K. Ando, S. Maekawa, and E. Saitoh, Observation of spin Seebeck effect, *Nature (London)* **455**, 778 (2008).
- [15] S. S. Costa and L. C. Sampaio, Recent progress in the spin Seebeck and spin Peltier effects in insulating Magnets, *J. Mag. Mag. Mat.* **547**, 168773 (2022).
- [16] S. M. Rezende, R. L. Rodríguez-Suárez, R. O. Cunha, A. R. Rodrigues, F. L. A. Machado, G. A. Fonseca Guerra, J. C. Lopez Ortiz, and A. Azevedo, Magnon spin-current theory for the longitudinal spin-Seebeck effect, *Phys. Rev. B* **89**, 014416 (2014).
- [17] S. R. Boona, R. C. Myers, and J. P. Heremans, Spin caloritronics, *Energy Environ. Sci.* **7**, 885 (2014).
- [18] K. Uchida, M. Ishida, T. Kikkawa, A. Kirihara, T. Murakami, and E. Saitoh, Longitudinal spin Seebeck effect: From fundamentals to applications, *J. Phys.: Condens. Matter* **26**, 343202 (2014).
- [19] H. Yu, S. D. Brechet, and J.-P. Ansermet, Spin caloritronics, origin and outlook, *Phys. Lett. A* **381**, 825 (2017).
- [20] S. M. Rezende, R. L. Rodríguez-Suárez, and A. Azevedo, Magnon diffusion theory for the spin Seebeck effect in ferromagnetic and antiferromagnetic insulators, *J. Phys. D: Appl. Phys.* **51**, 174004 (2018).
- [21] S. M. Rezende, *Fundamentals of Magnonics, Lecture Notes in Physics 969* (Springer, Cham 2020).
- [22] K.-I. Uchida, Spin caloritronics, in *Materials Science and Materials Engineering* (Elsevier, Amsterdam, 2022).
- [23] A. Brataas, B. Van. Wess, O. Klein, G. de Loubens, M. Viret, Spin insulatronics, *Phys. Rep.* **885**, 1 (2020).
- [24] T. Kikkawa and E. Saitoh, Spin Seebeck effect: Sensitive probe for elementary excitation, spin correlation, transport, magnetic order, and domains in solids, *Annu. Rev. Condens. Matter Phys.* **14**, 129 (2023).
- [25] P. Chandra and P. B. Littlewood, A Landau primer for ferroelectrics, in *Physics of Ferroelectrics* (Springer, Berlin, Heidelberg, 2007), pp. 69–116.
- [26] N. A. Spaldin, Analogies and differences between ferroelectrics and ferromagnets, in *Physics of Ferroelectrics*, edited by K. M. Rabe, C. H. Ahn, and J.-M. Triscone (Springer, Berlin, 2007), pp. 175.
- [27] G. E. W. Bauer, P. Tang, R. Iguchi, and K. Uchida, Magnonics vs. ferronics, *J. Magn. Magn. Mater.* **541**, 168468 (2022).
- [28] P. Tang, R. Iguchi, K.-i. Uchida, and G. E. W. Bauer, Thermoelectric polarization transport in ferroelectric ballistic point contacts, *Phys. Rev. Lett.* **128**, 047601 (2022).
- [29] P. Tang, R. Iguchi, K.-i. Uchida, and G. E. W. Bauer, Excitations of the ferroelectric order, *Phys. Rev. B* **106**, L081105 (2022).
- [30] B. L. Wooten, R. Iguchi, P. Tang, J. S. Kang, K.-i. Uchida, G. E. W. Bauer, and J. P. Heremans, Electric field-dependent phonon spectrum and heat conduction in ferroelectrics, *Sci. Adv.* **9**, eadd7194 (2023).
- [31] X. Zhou, P. Tang, R. L. Rodríguez-Suárez, S. M. Rezende, G. E. W. Bauer, and T. Yu, Surface ferron excitations in ferroelectrics and their directional routing, *Chin. Phys. Lett.* **40**, 087103 (2023).
- [32] G. E. W. Bauer, P. Tang, R. Iguchi, J. Xiao, K. Shen, Z. Zhong, T. Yu, S. M. Rezende, J. P. Heremans, and K. Uchida, Polarization transport in ferroelectrics, *Phys. Rev. Appl.* **20**, 050501 (2023).
- [33] M. Z. Hasan and C. L. Kane, Colloquium: Topological insulators, *Rev. Mod. Phys.* **82**, 3045 (2010).
- [34] X.-L. Qi and S.-C. Zhang, Topological insulators and superconductors, *Rev. Mod. Phys.* **83**, 1057 (2011).
- [35] L. Fu, Topological crystalline insulators, *Phys. Rev. Lett.* **106**, 106802 (2011).
- [36] T. H. Hsieh, H. Lin, J. Liu, W. Duan, A. Bansil, and L. Fu, Topological crystalline insulators in the SnTe material class, *Nat. Commun.* **3**, 982 (2012).
- [37] Y. Ando, Topological insulator materials, *J. Phys. Soc. Jpn.* **82**, 102001 (2013); J. Wang and S.-C. Zhang, Topological states of condensed matter, *Nat. Mater.* **16**, 1062 (2017).
- [38] F. Katmis *et al.*, A high-temperature ferromagnetic topological insulating phase by proximity coupling, *Nature (London)* **533**, 513 (2016); T. Zhang, Y. Jiang, Z. Song, H. Huang, Y. He, Z. Fang, H. Weng, and C. Fang, Catalogue of topological electronic materials, *ibid.* **566**, 475 (2019).
- [39] M. G. Vergniory, L. Elcoro, C. Felser, N. Regnault, B. A. Bernevig, and Z. Wang, A complete catalogue of high-quality topological materials, *Nature (London)* **566**, 480 (2019).
- [40] A. Ryota, K. Fujisawa, T. Yamaguchi, R. Ishikawa, and S. Kuroda, Two-dimensional quantum transport of multivalley (111) surface state in topological crystalline insulator SnTe thin films, *Nano Res.* **9**, 490 (2016).
- [41] K. Chang *et al.*, Discovery of robust in-plane ferroelectricity in atomic-thick SnTe, *Science* **353**, 274 (2016).
- [42] C. D. O'Neill, D. A. Sokolov, A. Hermann, A. Bossak, C. Stock, and A. D. Huxley, Inelastic x-ray investigation of the ferroelectric transition in SnTe, *Phys. Rev. B* **95**, 144101 (2017).
- [43] S. Ohya, A. Yamamoto, T. Yamaguchi, R. Ishikawa, R. Akiyama, L. D. Anh, S. Goel, Y. K. Wakabayashi, S. Kuroda, and M. Tanaka, Observation of the inverse spin Hall effect in the topological crystalline insulator SnTe using spin pumping, *Phys. Rev. B* **96**, 094424 (2017).

- [44] K. Zou *et al.*, Revealing surface-state transport in ultrathin topological crystalline insulator SnTe films, *APL Mater* **7**, 051106 (2019).
- [45] J. Sławińska, F. T. Cerasoli, P. Gopal, M. Costa, S. Curtarolo, and M. B. Nardelli, Ultrathin SnTe Films as a route towards all-in-one spintronics devices, *2D Mater.* **7**, 025026 (2020).
- [46] W. Han, Y. C. Otani, and S. Maekawa, Quantum materials for spin and charge conversion, *npj Quantum Mater.* **3**, 27 (2018).
- [47] Y. Ando and M. Shiraishi, Spin to charge interconversion phenomena in the interface and surface states, *J. Phys. Soc. Jpn.* **86**, 011001 (2017).
- [48] H. Wang, P. Gopal, S. Picozzi, S. Curtarolo, M. B. Nardelli, and J. Sławińska, Spin Hall effect in prototype Rashba ferroelectrics GeTe and SnTe, *npj Comput. Mater.* **6**, 7 (2020).
- [49] S. Picozzi, Ferroelectric Rashba semiconductors as a novel class of multifunctional materials, *Front. Phys.* **2**, 10 (2014).
- [50] J. E. Hirsch, Spin Hall effect, *Phys. Rev. Lett.* **83**, 1834 (1999).
- [51] E. Saitoh, M. Ueda, H. Miyajima, and G. Tatara, Conversion of spin current into charge current at room temperature: Inverse spin-Hall effect, *Appl. Phys. Lett.* **88**, 182509 (2006).
- [52] A. Hoffmann, Spin Hall effects in metals, *IEEE Trans. Mag.* **49**, 5172 (2013).
- [53] J. Sinova, S. O. Valenzuela, J. Wunderlich, C. H. Back, and T. Jungwirth, Spin Hall effects, *Rev. Mod. Phys.* **87**, 1213 (2015).
- [54] Y. Tserkovnyak, A. Brataas, and G. E. W. Bauer, Spin pumping and magnetization dynamics in metallic multilayers, *Phys. Rev. B* **66**, 224403 (2002).
- [55] A. Azevedo, L. H. Vilela Leão, R. L. Rodriguez-Suarez, A. B. Oliveira, and S. M. Rezende, DC effect in ferromagnetic resonance: Evidence of the spin-pumping effect? *J. Appl. Phys.* **97**, 10C715 (2005).
- [56] Y. Tserkovnyak, A. Brataas, G. E. W. Bauer, and B. I. Halperin, Nonlocal magnetization dynamics in ferromagnetic heterostructures, *Rev. Mod. Phys.* **77**, 1375 (2005).
- [57] O. Mosendz, V. Vlaminck, J. E. Pearson, F. Y. Fradin, G. E. W. Bauer, S. D. Bader, and A. Hoffmann, Detection and quantification of inverse spin Hall effect from spin pumping in permalloy/normal metal bilayers, *Phys. Rev. B* **82**, 214403 (2010).
- [58] K. Ando, J. Ieda Takahashi, Y. Kajiwara, H. Nakayama, T. Yoshino, K. Harii, Y. Fujikawa, M. Matsuo, S. Maekawa, and E. Saitoh, Inverse spin-Hall effect induced by spin pumping in metallic system, *J. Appl. Phys.* **109**, 103913 (2011).
- [59] A. Azevedo, L. H. Vilela-Leão, R. L. Rodríguez-Suárez, A. F. Lacerda Santos, and S. M. Rezende, Spin pumping and anisotropic magnetoresistance voltages in magnetic bilayers: Theory and experiment, *Phys. Rev. B* **83**, 144402 (2011).
- [60] E. I. Rashba, Semiconductors with a loop of extrema, *J. Electron Spectros. Related Phenomena* **201**, 4 (2015).
- [61] Y. A. Bychkov and E. I. Rashba, Oscillatory effects and the magnetic susceptibility of carriers in inversion layers, *J. Phys. C: Solid State Phys.* **17**, 6039 (1984).
- [62] V. M. Edelstein, Spin polarization of conduction electrons induced by electric current in two-dimensional asymmetric electron systems, *Solid State Commun.* **73**, 233 (1990).
- [63] J. C. Rojas-Sánchez, L. Vila, G. Desfonds, S. Gambarelli, J. P. Attané, J. M. De Teresa, C. Magén, and A. Fert, Spin-to-charge conversion using Rashba coupling at the interface between non-magnetic materials, *Nat. Commun.* **4**, 2944 (2013).
- [64] A. Manchon, H. C. Koo, J. Nitta, S. M. Frolov, and R. A. Duine, New perspectives for Rashba spin-orbit coupling, *Nat. Mater.* **14**, 871 (2015).
- [65] J. B. S. Mendes, O. Alves Santos, L. M. Meireles, R. G. Lacerda, L. H. Vilela-Leão, F. L. A. Machado, R. L. Rodríguez-Suárez, A. Azevedo, and S. M. Rezende, Spin-to-charge-current conversion and magnetoresistance in yttrium iron garnet-graphene hybrid structure, *Phys. Rev. Lett.* **115**, 226601 (2015).
- [66] S. Sangiao, J. M. De Teresa, L. Morellon, I. Lucas, M. C. Martínez-Velarte, and M. Viret, Control of the spin to charge conversion using the inverse Rashba-Edelstein effect, *Appl. Phys. Lett.* **106**, 172403 (2015).
- [67] A. Soumyanarayanan, N. Reyren, A. Fert, and C. Panagopoulos, Emergent phenomena induced by spin-orbit coupling at surfaces and interfaces, *Nature (London)* **539**, 509 (2016).
- [68] S. Zhang and A. Fert, Conversion between spin and charge currents with topological insulators, *Phys. Rev. B* **94**, 184423 (2016).
- [69] J.-C. Rojas-Sánchez *et al.*, Spin to charge conversion at room temperature by spin pumping into a new type of topological insulator: A-Sn Films, *Phys. Rev. Lett.* **116**, 096602 (2016).
- [70] K. Kondou, R. Yoshimi, A. Tsukazaki, Y. Fukuma, J. Matsuno, K. S. Takahashi, M. Kawasaki, Y. Tokura, and Y. Otani, Fermi-level-dependent charge-to-spin current conversion by Dirac surface states of topological insulators, *Nat. Phys.* **12**, 1027 (2016).
- [71] M. Matsushima, Y. Ando, S. Dushenko, R. Ohshima, R. Kumamoto, T. Shinjo, and M. Shiraishi, Quantitative investigation of the inverse Rashba-Edelstein effect in Bi/Ag and Ag/Bi on YIG, *Appl. Phys. Lett.* **110**, 072404 (2017).
- [72] J. B. S. Mendes, O. A. Santos, J. Holanda, R. P. Loreto, C. I. L. De Araujo, C.-Z. Chang, J. S. Moodera, A. Azevedo, and S. M. Rezende, Dirac-surface-state-dominated spin to charge current conversion in the topological insulator $(\text{Bi}_{0.22}\text{Sb}_{0.78})_2\text{Te}_3$ films at room temperature, *Phys. Rev. B* **96**, 180415(R) (2017).
- [73] J. B. S. Mendes, A. Aparecido-Ferreira, J. Holanda, A. Azevedo, and S. M. Rezende, Efficient spin to charge current conversion in the 2D semiconductor MoS_2 by spin pumping from yttrium iron garnet, *Appl. Phys. Lett.* **112**, 242407 (2018).
- [74] J.-C. Rojas-Sánchez and A. Fert, Compared efficiencies of conversions between charge and spin current by spin-orbit interactions in two- and three-dimensional systems, *Phys. Rev. Appl.* **11**, 054049 (2019).
- [75] D. C. Mahendra, T. Liu, J.-Y. Chen, T. Peterson, P. Sahu, H. Li, Z. Zhao, M. Wu, and J.-P. Wang, Room-temperature spin-to-charge conversion in sputtered bismuth selenide thin films via spin pumping from yttrium iron garnet, *Appl. Phys. Lett.* **114**, 102401 (2019).
- [76] J. Cheng, B. F. Miao, Z. Liu, M. Yang, K. He, Y. L. Zeng, H. Niu, X. Yang, Z. Q. Wang, X. H. Hong, S. J. Fu, L. Sun, Y. Liu, Y. Z. Wu, Z. Yuan, and H. F. Ding, Coherent picture on the pure spin transport between Ag/Bi and ferromagnets, *Phys. Rev. Lett.* **129**, 097203 (2022).
- [77] E. Gomes da Silva, J. E. Abrão, E. S. Santos, S. Bedanta, H. F. Ding, J. B. S. Mendes, and A. Azevedo, Surface-state mediated spin-to-charge conversion in Sb films via bilateral spin current injection, *Appl. Phys. Lett.* **123**, 202402 (2023).
- [78] Y. Tserkovnyak, A. Brataas, and G. E. W. Bauer, Enhanced Gilbert damping in thin ferromagnetic films, *Phys. Rev. Lett.* **88**, 117601 (2002).

- [79] S. M. Rezende, R. L. Rodríguez-Suárez, and A. Azevedo, Magnetic relaxation due to spin pumping in thick ferromagnetic films in contact with normal metals, *Phys. Rev. B* **88**, 014404 (2013).
- [80] C. Hahn, G. de Loubens, O. Klein, M. Viret, V. V. Naletov, and J. Ben Youssef, Comparative measurements of inverse spin Hall effects and magnetoresistance in YIG/Pt and YIG/Ta, *Phys. Rev. B* **87**, 174417 (2013).
- [81] J. B. S. Mendes, R. O. Cunha, O. Alves Santos, P. R. T. Ribeiro, F. L. A. Machado, R. L. Rodríguez-Suárez, A. Azevedo, and S. M. Rezende, Large inverse spin Hall effect in the antiferromagnetic metal Ir₂₀Mn₈₀, *Phys. Rev. B* **89**, 140406 (2014).
- [82] D. M. Pozar, *Microwave Engineering* (John Wiley & Sons, New York 2012).
- [83] M. Gamino, R. O. Cunha, J. B. S. Mendes, S. M. Rezende, and A. Azevedo, Spin current detection in antiferromagnetic CuMnAs, *App. Phys. Lett.* **115**, 182407 (2019).
- [84] J. B. S. Mendes, A. S. Viera, R. O. Cunha, S. O. Ferreira, R. D. Reis, M. Schmidt, M. Nicklas, S. M. Rezende, and A. Azevedo, Efficient spin-to-charge interconversion in Weyl semimetal TaP at room temperature, *Adv. Mater. Interfaces* **9**, 2201716 (2022).
- [85] J. B. S. Mendes, O. Alves Santos, T. Chagas, R. Magalhães-Paniago, T. J. A. Mori, J. Holanda, L. M. Meireles, R. G. Lacerda, A. Azevedo, and S. M. Rezende, Direct detection of induced magnetic moment and efficient spin-to-charge conversion in graphene/ferromagnetic structures, *Phys. Rev. B* **99**, 214446 (2019).
- [86] J. B. S. Mendes, M. Gamino, R. O. Cunha, J. E. Abrão, S. M. Rezende, and A. Azevedo, Unveiling the spin-to-charge current conversion signal in the topological insulator Bi₂Se₃ by means of spin pumping experiments, *Phys. Rev. Mater.* **5**, 024206 (2021).
- [87] H. Wang, J. Kally, J. S. Lee, T. Liu, H. Chang, D. R. Hickey, K. A. Mkhoyan, M. Wu, A. Richardella, and N. Samarth, Surface-state-dominated spin-charge current conversion in topological-insulator–ferromagnetic-insulator heterostructures, *Phys. Rev. Lett.* **117**, 076601 (2016).